# Article

# Adsorption Properties of Magnetic CoFe$_2$O$_4$@SiO$_2$ Decorated with P4VP Applied to Bisphenol A

*Giuliana Valentini,[a] Natália B. Caon,[a] Fabrício Luiz Faita[b] and Alexandre Luis Parize* [ORCID] *,[a]*

*[a]Grupo de Estudos em Materiais Poliméricos (POLIMAT), Departamento de Química, Universidade Federal de Santa Catarina (UFSC), 88040-900 Florianópolis-SC, Brazil*

*[b]Laboratório de Altas Pressões e Materiais Avançados (LAPMA), Instituto de Física, Universidade Federal do Rio Grande do Sul (UFRGS), 90040-060 Porto Alegre-RS, Brazil*

In this study, the preparation and adsorption properties of cobalt ferrite core-shell nanoparticles coated with silica and decorated with poly(4-vinylpyridine) (CoFe$_2$O$_4$@SiO$_2$-P4VP) applied to bisphenol A (BPA) adsorption were described. The CoFe$_2$O$_4$-based core was coated by a nanometric layer of silica under Stöber conditions and followed by coating with poly(4-vinylpyridine) via surface polymerization in miniemulsion. The characterizations involved transmission electron microscopy (TEM), X-ray diffraction (XRD), vibrating sample magnetometer (VSM), Fourier transform infrared (FTIR), thermogravimetry (TGA), dynamic light scattering (DLS) and zeta potential. The polymeric core-shell nanoparticle showed a spherical structure with a magnetic core of ca. 11 nm and a layer of silica of ca. 4 nm. The amount of poly(4-vinylpyridine) that decorated the nanoparticle surface was verified by thermogravimetric analysis. CoFe$_2$O$_4$@SiO$_2$-P4VP exhibited the capacity to adsorb bisphenol A. The chemometric model indicated a significant effect between the ionic strength and pH of the solution in the adsorption of bisphenol A. CoFe$_2$O$_4$@SiO$_2$-P4VP presented a superior adsorption capacity towards BPA (46.6 mg g$^{-1}$) in optimized conditions. The adsorption kinetics of BPA by CoFe$_2$O$_4$@SiO$_2$-P4VP involved a pseudo-second order process. Also, the adsorption isotherm indicated a multilayer process with data well-adjusted by Freundlich equation. The nanomaterial CoFe$_2$O$_4$@SiO$_2$-P4VP can be reused in adsorption of BPA for up to eight cycles.

**Keywords:** adsorption, core-shell, nanoparticle, polymer

## Introduction

Bisphenol A (4.4'-(propane-2,2 diyl) diphenol), (BPA), is an emerging contaminant found in biosolids, soils and water sources due to its wide use in a variety of industrialized products such as plastics and epoxy resins, and it is not completely removed during wastewater treatment.[1] At neutral pH (p$K_a$ value ca. 9.6), BPA has high hydrophobicity and lipid permeability, which generate bioaccumulation in animals and microorganisms.[2] BPA is an endocrine disruptor detected in the body of animals and humans, where exposure can cause short- and long-term toxicity.[3] There are techniques to remove BPA from water, and among them, a technique that attracts attention is adsorption.[4-6]

Magnetic adsorption is a simple way to remove substances from the residual waters by removing the loaded adsorbent with a magnet. Adsorbents have high applicability because they are reusable materials and do not cause the decomposition of species susceptible to contamination.[7,8] When compared to other effluent remediation methods, magnetic adsorption has advantages such as easy handling and low cost. After the contact of the magnetic adsorbent with the contaminant, it is adsorbed on the adsorbent and separated from the solution with a magnetic separator. In an appropriate solvent, the contaminant is eluted and given the appropriate destination.[9,10] Thus, the development of nanomaterials with properties that act in magnetic adsorption is of current interest.

Nanocomposites are heterogeneous materials in which, unlike microcomposites, one of the phases has one, two, or three dimensions below 100 nm, or the composite phases have nanoscale distances between them.[7,11] Besides this

characteristic, they present combined properties from the matrix and from the nanomaterial, which results in a functional material.[12] In this context, core-shell nanoparticles are formed by an internal material (core) and an external layer (shell).[13] The composition of the shell is highly dependent on the final application of the nanocomposite.[12] The silica matrix consists of a versatile material for chemical functionalization, and seed-mediated growth is the most common technique employed to achieve a silica shell in a nanoparticle core.[14] In the Stöber method, tetraethylorthosilicate (TEOS) or other organosilanes are combined in water, ethanol and ammonia, under stirring, to form particles with a size that depends on the concentration of the solvents and the silicates.[15]

The modification of silanol groups is often required to prevent adsorption of basic analytes that could compromise the recovery of the adsorbent.[16] Polymer deposition can be applied for the pretreatment of hydrophobic and hydrophilic analytes.[17]

In recent years, poly(4-vinylpyridine) (P4VP) has attracted the attention of researchers due to its special functional properties, such as pH-responsive characteristics in aqueous solution and good affinity for metals and organic contaminants.[18,19] P4VP can be prepared via thermally initiated free-radical polymerization of 4-vinylpyridine (4VP). The deposition of the P4VP onto a magnetic core can be carried out by polymerization in a miniemulsion under an inert atmosphere and heating through polymeric growth on the nanoparticulate surface.[18-20] In addition, P4VP has flexible polymer chains that may act as a stabilizer after coating on the surface and producing resultant composite materials with good stability.[18,20] Magnetic composites with P4VP and magnetic nanoparticles promote effective adsorption due to the high surface area and interactions with the polymer. These composites can be easily removed from the solution using an external magnetic field (magnet), avoiding centrifugation and filtration processes.[20,21]

Combining the preparation of the adsorbent oriented to the targeted adsorbates with chemometric optimization provides ideal conditions to achieve the highest performance of the adsorbent.[22] The univariate optimization of magnetic adsorption parameters is the type most found in the literature. However, univariate conditions lead to many experiments and inhibit the visualization of synergistic effects between the factors. The multivariate strategy requires the optimization of a condition with the smallest possible number of experiments that allows visualization of the interactions between the factors.[10,23] The response surface method (RSM) is often used to optimize processes. The factorial experimental design associated with RSM provides process information, reducing the number of empirical solutions, which involve trial and error. Among the advantages are the reduction in the number of experiments and the possibility of evaluating the effects of interaction between the factors (variables).[22,24]

So, this present study reports the preparation of core-shell magnetic nanoparticles coated with silica and P4VP for adsorption of the emerging contaminant bisphenol A in water. The proposal involves a magnetic core based on cobalt ferrite, and the shell consists of a layer of silica of controlled thickness with a polymeric coating. The magnetic core is necessary to provide the magnetic response under an external magnetic field. The shell material is designed to promote the adsorption of BPA by van der Waals forces and hydrogen bonds. The coating of the magnetic nanoparticles with silica was carried out by an eco-friendly route of silica coating and polymerization in miniemulsion using aqueous medium and inert atmosphere. The adsorption capacity of the prepared nanomaterial was verified. Using a response surface, it was possible to optimize the adsorption conditions by evaluating the synergism between the pH and ionic strength variables. The nanomaterial was evaluated for the kinetics, balance, and thermodynamics of the adsorption process, as well as the desorption solvent and the reuse cycles.

## Experimental

### Chemicals

Type 1 ultrapure water (18.2 MΩ cm at 25 °C) was used throughout all experimental procedures. Iron(III) chloride anhydrous (FeCl$_3$ 98%); iron(II) chloride tetrahydrate (FeCl$_2$.4H$_2$O ≥ 99%); sodium hydroxide (NaOH 97%); hydrochloric acid (HCl 37%); acetonitrile (CH$_3$CN ≥ 99.9%); citric acid (C$_6$H$_8$O$_7$ 99.5%); bisphenol A (C$_{15}$H$_{16}$O$_2$ 99.7%), divinylbenzene (DVB C$_8$H$_8$ 80%), potassium persulfate (KPS), polyvinylpyrrolidone (PVP) and 4-vinylpiridine (4-VP C$_7$H$_7$N 95%) were purchased from Sigma-Aldrich (St. Louis, USA). The silica precursor tetraethylorthosilicate (TEOS C$_8$H$_{20}$O$_4$Si 98%) was purchased from Acros Organics (São Paulo, Brazil). Cobalt(II) chloride hexahydrate (CoCl$_2$.6H$_2$O 98.5%); iron(III) nitrate nonahydrate (Fe(NO$_3$)$_3$.9H$_2$O 99.5%); ammonium hydroxide P.A. (NH$_4$OH 30%); acetone P.A. (C$_3$H$_6$O 99.6%), nitric acid (HNO$_3$ 65%) and ethanol (C$_2$H$_5$OH 99.8%) were purchased from Neon® (Neon, Suzano, SP, Brazil). All chemicals were used without further purification and were of analytical grade. NdFeB cubic magnets (10 mm length, grade N50) were purchased from IMASHOP (São Paulo, Brazil).

## Preparation of cobalt ferrite ferrofluid

Cobalt ferrite ($CoFe_2O_4$) was synthesized according to the procedure previously described by Caon *et al.*[24] In general, 0.30 mol of $FeCl_3$ and 0.15 mol of $CoCl_2.6H_2O$ were dissolved under heating in 300 mL of acidic solution (10% v/v HCl). The mixture was added to 1.5 L of boiling 2.0 mol $L^{-1}$ NaOH and kept under stirring and heating (ca. 90 °C) for 120 min. Magnetic separation was employed to separate the solid from the solution. The solid was washed with water to neutral pH. Approximately 200 mL of 1.0 mol $L^{-1}$ $HNO_3$ solution was added and kept under stirring for 20 min. The supernatant was separated with the aid of a magnet and 200 mL of the 1.0 mol $L^{-1}$ Fe $(NO_3)_3.9H_2O$ aqueous solution was placed in contact with the solid, under heating and stirring. The system was kept boiling for 30 min, followed by magnetic separation of the solid. Acetone was used to remove excess of ferric nitrate. Water was added to the system after evaporation of acetone to obtain a ferrofluid.

## Growth of silica shell

The silica coating was carried out similarly to Pinho *et al.*[25] An aliquot of ferrofluid was washed with 0.1 mol $L^{-1}$ citric acid to increase the stable pH range. The magnetic content was separated with the aid of a magnet and again dispersed in 1 L of a mixture of ethanol, water and ammonia (75:23.5:1.5 v:v:v), under mechanical stirring. The authors reported a controllable silica shell, adjusted by the amount of TEOS in the reaction medium, calculated using equation 1.[24,25]

$$V_{TEOS} = N_{part}\left[\left(\frac{\rho_{SiO_2}}{M_{TEOS}}\right)/\left(M_{SiO_2}\rho_{TEOS}\right)\right]\left[\frac{4}{3}\pi\left(\left(r+e_{shell}\right)^3 - r^3\right)\right] \quad (1)$$

The predicted silica shell thickness is $e_{shell}$ (the difference $\left[\frac{4}{3}\pi\left(\left(r+e_{shell}\right)^3 - r^3\right)\right]$ corresponds to the volume of the silica shell), $\rho_{SiO_2}$ and $M_{SiO_2}$ are density and molar weight of silica. $V_{TEOS}$, $\rho_{TEOS}$, $M_{TEOS}$ are volume, density, and molar weight of TEOS. $N_{part}$ is the number of particles, which considers the density, molar weight, and mean radius of the nanoparticle.

Using equation 1, the amount of TEOS was calculated to achieve a shell of about 2 nm thick, with 2.54 mL for $CoFe_2O_4$ to calculate $N_{part}$ of 1.0 g of $CoFe_2O_4$. The particles were considered to have a spherical shape. The volume of 1 single $CoFe_2O_4$ nanoparticle was calculated using the mean diameter from X-ray diffraction (XRD).[26] Using the density of the $CoFe_2O_4$ taken from the literature, the volume of 1.0 g of $CoFe_2O_4$ was calculated. The division of

the volume of 1.0 g of $CoFe_2O_4$ by the volume of 1 single $CoFe_2O_4$ resulted in the $N_{part}$. After the amount of TEOS had been added dropwise for 10 min, the system was stirred (400 rpm) for 12 h.

## 4-Vinylpiridine polymerization on the silica surface

The decoration of the silica surface using P4VP was achieved according to the procedure described by Miao *et al.*[20] with modifications. The process was carried out for $CoFe_2O_4@SiO_2$, where about 0.1 g of nanoparticle was dispersed in 100 mL of polyvinylpyrrolidone (PVP) 0.15% (m/v) under ultrasonication for 30 min. The suspension was mixed in an emulsion of 4-vinylpyridine (4VP) (0.125 g) and divinylbenzene (DVB) (0.125 g) in aqueous solution (20 mL) containing PVP (0.05 g) obtained mechanically in Ultra-Turrax® (model IKA® T125) at 8000 rpm for 40 min. Then, a mixture was added to a flask with three entries. The suspension remained in mechanical stirring for 2 h under a nitrogen atmosphere at 70 °C, with the mechanical stirrer model RW 20 IKA, with glass rush and teflon blades, coupled to avoid the agglomeration of nanoparticles that could be induced by magnetism. After this period, polymerization of 4VP was achieved using potassium persulfate (KPS) (10 mg). After 6 h, the nanomaterials were decanted with the aid of a NdFeB magnet and washed with ultrapure $H_2O$ and ethanol to terminate the reaction. The washing process was repeated 3 times. The supernatant containing the nanomaterials was then dried in an air circulation oven at 60 °C for 12 h.[18,20]

## Characterization of the prepared nanomaterials

Size and morphology were evaluated by transmission electron microscopy (TEM), using a JEM-2100 (JEOL) (Tokyo, Japan) microscope at an acceleration voltage of 100 kV. Particle size distribution was obtained considering a log-normal distribution of spherical-shaped particles, using ImageJ.[27,28]

The structural properties were investigated by X-ray diffraction (XRD) for all prepared powder samples using a Rigaku Ultima-IV (Mumbai, India) diffractometer with Cu Kα radiation (λ = 0.15418 nm) at a generator voltage of 40 kV and a generator current of 25 mA. The diffractograms were recorded at θ-2θ mode in continuous scanning from 15 to 75° at 2θ. The mean crystallite size for all samples was obtained by applying the Scherrer equation (equation 2) to the most intense peak.

$$D = \frac{k\lambda}{\beta\cos(\theta)} \quad (2)$$

where D is the crystallite size, λ is the X-ray wavelength, β is the width of the peak after correcting for instrumental peak broadening (β expressed in radians), θ is the Bragg angle and k is the Scherrer constant.[24,26]

The magnetic properties were investigated by using an EZ9 MicroSense vibrating sample magnetometer (VSM) (Darmstadt, Germany) at room temperature with a magnetic field (H) cycled between −20 and +20 kOe. The magnetic content of nanocomposites was verified by equation 3.

$$\text{Magnetic content}\,(\text{wt.\%}) = \frac{M_s}{M_{s_0}} \times 100 \qquad (3)$$

where $M_s$ is the saturation magnetization for the composites and $M_{s_0}$ is the saturation magnetization for the pure nanoparticle.[24]

Infrared spectroscopy provided Fourier transform infrared (FTIR) spectra that were acquired using KBr pellets in the spectral range of 4000-400 cm⁻¹, resolution 2 cm⁻¹, 64 acquisitions, on a Shimadzu IRPrestige-21 (Japan).[26] Thermogravimetry (TGA) curves were acquired on a Shimadzu TGA-50 (Kyoto, Japan) thermogravimetric analyzer using platinum cell, under N₂ atmosphere (50 mL min⁻¹), from 25 to 800 °C, heating rate of 10 °C min⁻¹.[24,26]

Zeta potential and hydrodynamic radius using dynamic light scattering (DLS) for the aqueous dispersions (filtered previously using 0.2 μm cellulose acetate filter) of CoFe₂O₄ (pH 4.0) and the analogs CoFe₂O₄@SiO₂ and CoFe₂O₄@SiO₂-P4VP (pH 6.0)[24] were measured using Malvern Instruments Zetasizer Nano Series (Malvern Instruments, UK), equipped with a laser source of 633 nm. Zeta potential of CoFe₂O₄@SiO₂-P4VP was also evaluated as a function of pH to assess colloidal stability in the range analyzed in the adsorption experimental planning.

## Adsorption of bisphenol A

### Response surface

The initial approach was to define which factors were of interest. The literature was consulted, and the factors of interest selected for optimization were the ionic strength and pH of the solution (independent factors).[23] The response variable considered was the adsorption capacity ($Q_e$). Statistical analyses were performed using StatSoft Statistica software version 13.5.0.17.[29] A central composite experimental design with 2 factors was developed to assess which factors effectively affect the adsorption of BPA and to define an appropriate condition for adsorption of the emerging contaminant. Table S1 (Supplementary Information (SI) section) shows the

codification of the factors used in the experimental design. Thirteen experiments were carried out with variation of all factors, as shown in Table S1, with triplicate of the central point. The following buffers (final concentration in the sample = 0.01 mol L⁻¹) were used at each pH level: buffer citrate to pH 3.88, acetate buffer to pH 4.5, phosphate buffer to pH 6.0, tris buffer to pH 7.5 and phosphate buffer to pH 8.12. The mass of adsorbent and the volume of solution were kept constant, at 5 mg and 10 mL, respectively.

The adsorption capacity response was calculated using equation 4:

$$Q_e = \frac{(C_i - C_e)V}{m} \qquad (4)$$

where $Q_e$ refers to the adsorption capacity (mg g⁻¹), $C_i$ refers to the initial concentration of the contaminant (100 mg L⁻¹), $C_e$ to the concentration of the contaminant in the equilibrium (in mg L⁻¹), V is the volume of solution (L) and m is the mass of adsorbent (g).[3,21] After being agitated at 200 rpm for 120 min, the adsorbent was separated by magnet. The supernatant was filtered by 0.22 μm filter membrane and determined by UV-Vis spectrophotometry (UV NOVA/1800, Brazil). The concentration of BPA was determined by UV-Vis at 277 nm. Data analysis was performed using StatSoft Statistica software version 13.5.0.17.[29]

### Optimization of adsorption time

Under conditions of optimized pH and ionic strength ([BPA]ᵢ = 100 mg L⁻¹, pH = 7.15; [NaCl] = 1.71 mol L⁻¹) to verify a proper time of adsorption after sonication, the adsorption capacity of the nanomaterial was verified after 1, 2, 3, 4, 5, 10, 15, 20, 25, 30, 50, 70 and 120 min of shaking (200 rpm) at 25 °C. The adsorption capacity at different times was evaluated using the pseudo-first order, pseudo-second order, Elovich and intraparticle dissemination models (equations 5, 6, 7 and 8).

$$Q_t = Q_e \left(1 - e^{k_1 t}\right) \qquad (5)$$

$$Q_t = \frac{Q_e^2 k_2 t}{k_2 Q_e \left(t + 1\right)} \qquad (6)$$

$$Q_t = \frac{\ln(\beta\alpha)}{\beta} + \frac{\ln(t)}{\beta} \qquad (7)$$

$$Q_t = k_{id} t^{1/2} + CL \qquad (8)$$

The pseudo-first order equation is one of the equations most used to evaluate the processes of adsorption of the

solute from a liquid solution, based on the adsorption capacity of the solid,[30,31] where $Q_e$ (mg g$^{-1}$) is the equilibrium adsorption capacity, $Q_t$ (mg g$^{-1}$) is the adsorption capacity at a given time, $k_1$ (min$^{-1}$) is the adsorption rate constant and t is the adsorption time. The pseudo-second order kinetic model is also based on the adsorption capacity of the solid phase. Where $k_2$ (g mg$^{-1}$ min$^{-1}$) is the adsorption rate constant, $Q_e$ (mg g$^{-1}$) is the concentration of solute adsorbed at equilibrium, and $Q_t$ (mg g$^{-1}$) is the concentration of the solute on the surface of the adsorbent. The kinetic model of intraparticle diffusion can be described in three steps.[6,32,33] The Elovich equation represented by equation 7 is used for systems that have heterogeneous surfaces, where β is the desorption constant (g mg$^{-1}$), α is the initial rate of adsorption (mg g$^{-1}$ min$^{-1}$) and qt is the amount adsorbed (mg g$^{-1}$) at time t (min).[28,34,35]

The intraparticle model (equation 8) represents the migration of the adsorbate present in the solution to the surface of the adsorbent. This movement of the solute occurs by molecular diffusion, where $k_{id}$ (g mg$^{-1}$ min$^{-1/2}$) is the intraparticle diffusion constant and CL (mg g$^{-1}$) is the boundary layer effect thickness.[32,36]

### Equilibrium adsorption

To get an insight into the adsorption behavior, the adsorption thermodynamics was calculated. Five mg of CoFe$_2$O$_4$@SiO$_2$-P4VP (0.50 g L$^{-1}$) were dispersed in BPA aqueous solution (100 mg L$^{-1}$, pH = 7.15; [NaCl] = 1.71 mol L$^{-1}$) at 25 °C and shaken at 300 rpm for 20 min. The adsorption equilibrium concentrations in different initials of BPA were evaluated through the Langmuir, Temkin and Freundlich models (equation 9, 10 and 11).

$$Q_e = \frac{Q_{max} K_L C_e}{1 + K_L C_e} \qquad (9)$$

$$Q_e = b_T \ln\left(K_T C_e\right) \qquad (10)$$

$$Q_e = K_F C_e^n \qquad (11)$$

The Langmuir isothermal (equation 9) model was one of the pioneers in the study of adjusted adsorption, where $K_L$ (L mg$^{-1}$) is the affinity constant, $Q_e$ (mg g$^{-1}$) represents the amount adsorbed, $Q_{max}$ (mg g$^{-1}$) is the maximum amount adsorbed and $C_e$ (mg L$^{-1}$) is the equilibrium concentration in the solution.[32,37-39] The Temkin isothermal model (equation 10) takes into account adsorbate-adsorbate interactions and does not account for extreme concentrations. Thus, for this model, the heat of adsorption of all molecules decreases linearly as the adsorbate covers the adsorbent. $K_T$ (L g$^{-1}$) is the equilibrium bond constant and $b_T$ is the Temkin constant.[6,31,40] Another model widely used in

adsorption studies is the Freundlich isotherm (equation 11). This isotherm corresponds to a distribution widely applied to heterogeneous systems, where $K_F$ [(mg g$^{-1}$)(L mg$^{-1}$)$^{1/n}$] is the Freundlich constant, representing the adsorption capacity of the solid, n is a parameter of the Freundlich equation related to the adsorption intensity. K and n are constants that depend on several experimental factors and are related to the distribution of active sites and the adsorbent adsorption capacity.[31-33,40]

### Desorption

Acetonitrile (ACN), ethanol (EtOH), dimethylformamide (DMF) and mixtures of these solvents following a simplex-lattice design with 10 experiments (triplicate of the central point) were employed to desorb the analyte from the nanomaterial.[23,35] After the adsorption step using the optimized adsorption time, the magnetic nanocomposite was separated from the solution using a NdFeB magnet and the supernatant was discarded. An amount of 2 mL of the evaluated solvent was poured on top of the solid and the system was sonicated for 20 min.[24] In the sequence, the nanomaterial was sonicated and separated, and the supernatant was collected and quantified using ultraviolet visible spectrophotometer.

### Nanomaterial reuse cycles

The stability of the nanomaterial was evaluated after 8 successive cycles of the procedures (adsorption/desorption) under optimized response surface conditions and adsorption time. Desorption was carried out using the conditions optimized in the desorption experiment.

## Results and Discussion

### Characterization of the nanomaterials

### Properties regarding size, structure, and morphology

The surface treatment of the magnetic nanoparticles with iron nitrate to improve chemical stability, preventing solubilization in acidic media, also provides a gain in the iron fraction. This treatment forms a shell that is mainly composed of amorphous ferric hydroxides and is of the order of a nanometer.[41]

Figure 1 shows the TEM images recorded for the CoFe$_2$O$_4$, CoFe$_2$O$_4$@SiO$_2$, CoFe$_2$O$_4$@SiO$_2$-P4VP samples with their respective diameter size distributions. TEM images (Figures 1a, 1c and 1e) show the nanoparticulated materials, with a distribution of diameter values that were well adjusted by a log-normal equation with a maximum value of around 10.2, 14.3 and 90.8 nm, respectively (Figures 1b, 1d and 1f).

For the core-shell CoFe$_2$O$_4$@SiO$_2$ nanocomposite, TEM images indicate that the thickness of the silica shell varied from the calculated value (2 nm) to the observed ca. 4 nm of SiO$_2$ thickness. The difference between the calculated and real thickness of the shell may be due to some aggregation of the bare nanoparticles during synthesis, which led to a greater SiO$_2$ thickness than the calculated value. Similar results were reported by Pinho *et al.*,[25] where the same route was employed to create a silica shell over maghemite nanoparticles.[25] The authors also verified deviation to a greater-than-estimated shell thickness.

XRD and DLS also provided the diameter of the particles. The values were distinct from the values obtained by TEM analysis (see Table 1); in fact, each technique reveals different aspects of the particles. Briefly, TEM shows most atomically dense regions of the dried samples (mainly core-shell system). XRD (Figure 2a) shows only the crystalline parts (mainly the crystalline core) and DLS (Figure 2b) reveals information about all regions of the sample that are able to scatter light in solution (core-shell-polymer system).[24]

TEM measurements were carried out in a high vacuum, and the samples were completely free of water. Thus, without water between the polymeric networks, the diameter of the particles is smaller than that found in the measurements in solution by DLS (see Figure 2b and Table 1). It is observed that the CoFe$_2$O$_4$@SiO$_2$ nanoparticle presents a great variation in d$^{TEM}$ when compared to d$^{DLS}$. In the work by Kevadiya *et al.*,[42] the silica layer showed similar values to those obtained here in both DLS (Table 1)
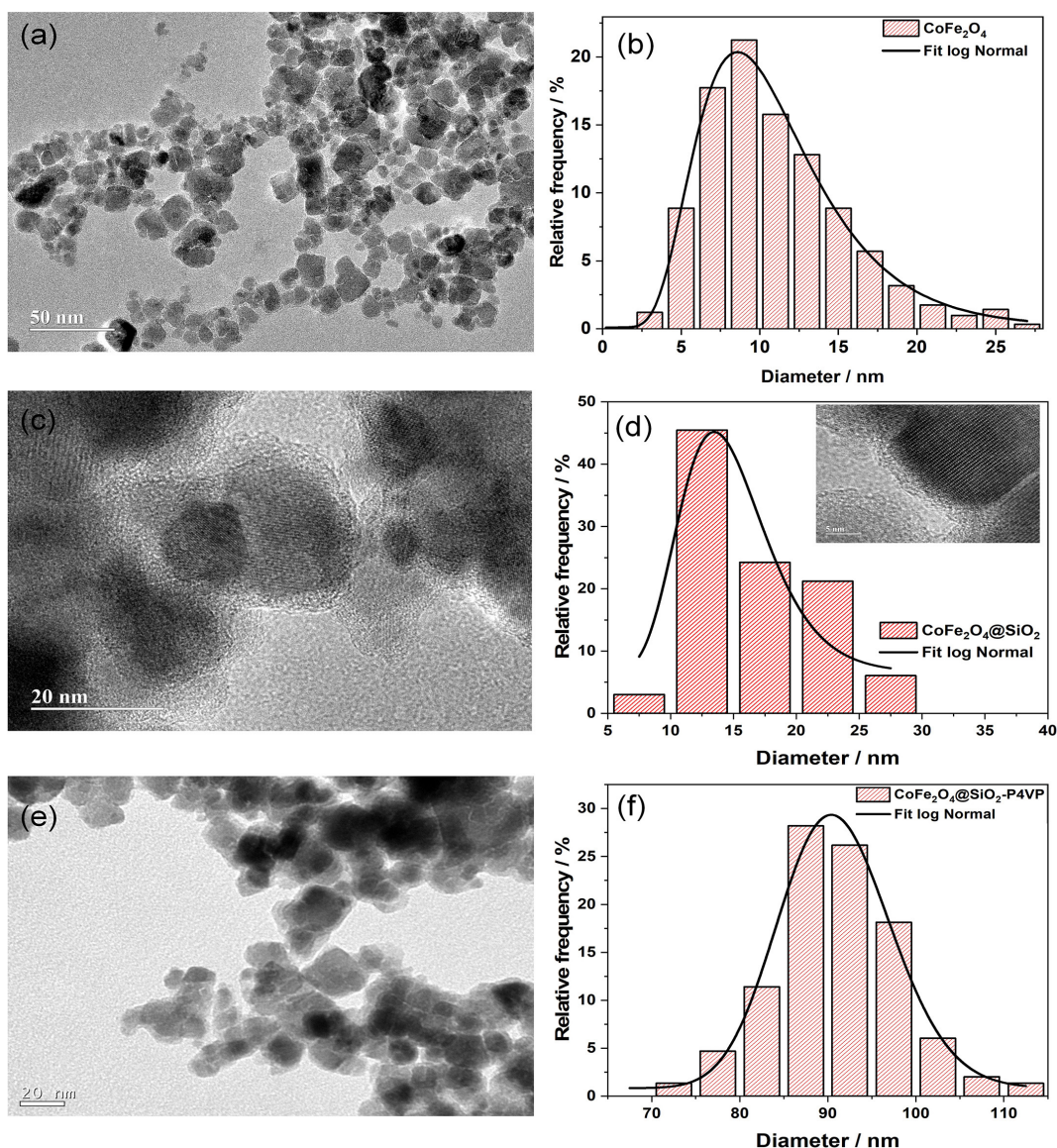


**Figure 1.** (a) TEM image and (b) size distribution for CoFe$_2$O$_4$. (c) TEM and (d) size distribution (and HRTEM) for CoFe$_2$O$_4$@SiO$_2$. (e) TEM and (f) size distribution for CoFe$_2$O$_4$@SiO$_2$-P4VP.

**Table 1.** Hydrodynamic diameter, diffusion coefficient, zeta potential, conductivity, polydispersity indices and magnetic parameters of $CoFe_2O_4$ (pH 4.0), $CoFe_2O_4@SiO_2$ (pH 6.0) and $CoFe_2O_4@SiO_2$-P4VP (pH 6.0)

| Sample | $d^{TEM}$ / nm | $d^{XRD}$ / nm | $d^{DLS}$ / nm | D / ($\mu m^2$ $s^{-1}$) | $\zeta$ / mV | $\Sigma$ / (mS $cm^{-1}$) | PDI | $M_S$ / (emu $g^{-1}$) | $M_R$ / (emu $g^{-1}$) | $H_C$ / Oe | $MC^{300K}$ / wt.% |
|---|---|---|---|---|---|---|---|---|---|---|---|
| $CoFe_2O_4$ | 10.2 ± 0.15 | 12.6 ± 0.3 | 30.4 ± 1.9 | 16.2 | +40.9 ± 1.9 | 0.091 | 0.175 | 58.7 | 15.1 | 426 | 100 |
| $CoFe_2O_4@SiO_2$ | 14.3 ± 1.7 | 13.6 ± 0.4 | 60.1 ± 3.0 | 8.2 | −30.1 ± 0.7 | 0.013 | 0.178 | 46.3 | 17.3 | 625 | 79.5 |
| $CoFe_2O_4@SiO_2$-P4VP | 90.8 ± 0.32 | 13.7 ± 0.4 | 109.9 ± 3.6 | 4.5 | −24.8 ± 1.2 | 0.011 | 0.317 | 25.6 | 7.9 | 522 | 41.8 |

$d^{TEM}$: diameter obtained by TEM; $d^{XRD}$: diameter obtained by XRD; $d^{DLS}$: diameter obtained by DLS; D: difusion coefficient; $\zeta$: zeta potencial; $\Sigma$: conductivity; PDI: polydispersity index; $M_S$: saturation magnetization; $M_R$: remanence magnetization; $H_C$: coercivity; $MC^{300K}$: magnetic content.

and TEM. In that article, the authors state that the diameter given by the DLS (Figure 2b) is associated with clusters of primary particles.[42]

The crystalline structure and the mean crystallite size ($d^{XRD}$) of the samples were evaluated by XRD measurements and the Scherrer equation (equation 2) from the most intense peak. Figure 2a shows the XRD patterns from $CoFe_2O_4$, $CoFe_2O_4@SiO_2$ and $CoFe_2O_4@SiO_2$-P4VP powder samples. All patterns showed diffraction peaks at 30.2°, 35.5°, 43.2°, 53.6°, 57.1° and 62.7°, assigned respectively to (2 2 0), (3 1 1), (4 0 0), (4 2 2), (5 1 1), (4 4 0) crystalline planes of cobalt iron ferrite phase (ICSD card No. 184063).[43] The mean crystallite size increased around 4 nm after the $SiO_2$ shell grew and remained practically unchanged after the P4VP layer had grown over the $CoFe_2O_4@SiO_2$ core. The values obtained for $d^{XRD}$ are shown in Table 1. The increase in the mean crystallite size observed can be attributed to the small amount of agglomeration before the $CoFe_2O_4$ nanoparticles were totally recovered from the $SiO_2$ layer. Additionally, the crystalline portion of the nanocomposite is not attacked by the reaction medium by P4VP functionalization. For the crystallography, the cell parameter and volume values obtained for both materials ($CoFe_2O_4@SiO_2$ and $CoFe_2O_4@SiO_2$-P4VP) were 8.4 Å and 585.5 Å³, respectively. These values, when compared to the data obtained by Ferreira *et al.*[44] show a deviation of 0.2 and 0.5%, respectively. This indicates that there are crystalline defects, but they are not predominant.[44]

The mean crystallite sizes were obtained without considering the contribution of microstrain and/or structural defects in the broadening of the XRD peaks. This may have generated slightly underestimated values. On the other hand, the Scherrer formula has a low divergence of values for the mean crystallite size range investigated in this work.[45]

From the deconvolution of DLS correlation curves (Figure 2b), the diameter values are significantly different from those obtained using TEM and XRD techniques (Table 1). This is due to the fact that the hydrodynamic radius is considered the radius of a sphere that presents the same diffusion coefficient (D) in a particular viscous environment as the ensemble of particles that are scattering the light.[46] The silica layer, despite being intentionally thin, can make hydrogen bonds more strongly and, therefore, the hydrodynamic diameter practically doubles with respect to the $CoFe_2O_4$ nanoparticles. As expected, $CoFe_2O_4@SiO_2$-P4VP had the largest hydrodynamic radius, as it has more layers on the particle surface. Furthermore, the particle size resembled that found by Clara-Rahola *et al.*,[47] who performed a study using P4VP with a gold nanoparticulate core.[47] When the pH is above 6, due to the absence of charges in the polymeric network, P4VP collapses, as it has its smallest possible diameter.[47]

The diameter of TEM and the hydrodynamic radius in the collapsed state in which the polymer is found is $d^{TEM}/d^{DLS} = 0.83$. This relationship is generally presented in nano systems characterized by a dense core and a lighter shell. This relationship portrays the nature of the mass distribution of $d^{TEM}$ and the dynamic nature of $d^{DLS}$, due to the random movement of the particle in the solvent.[47,48]

An amount of solvent and counter ions contributes to a bigger diameter when compared to $d^{TEM}$ and $d^{XRD}$ values (see Table 1). TEM provides the 'true diameter' (from a statistically small sample) and XRD provides a mean diameter size from the crystalline region due to the constructive interference of X-rays scattered by periodic lattice planes of a sample.[46,49]

## Assessment of polymerization and deposition of the P4VP on the surface of the magnetic nanoparticles

TGA curves of the nanomaterials based on $CoFe_2O_4$ are presented in Figure 2c where, for $CoFe_2O_4$ and $CoFe_2O_4@SiO_2$ samples, small and not so well-defined mass losses were observed. For the $CoFe_2O_4$ nanoparticle, the first mass loss (up to approx. 100 °C) refers to water evaporation. Between 140 to 270 °C, nitrate loss occurs, possibly with $NO_2$ output. Later, there is no significant mass variation.[24] For $CoFe_2O_4@SiO_2$, the first mass loss (up to ca. 100 °C) refers to the output of ethanol or water adsorbed on the silica
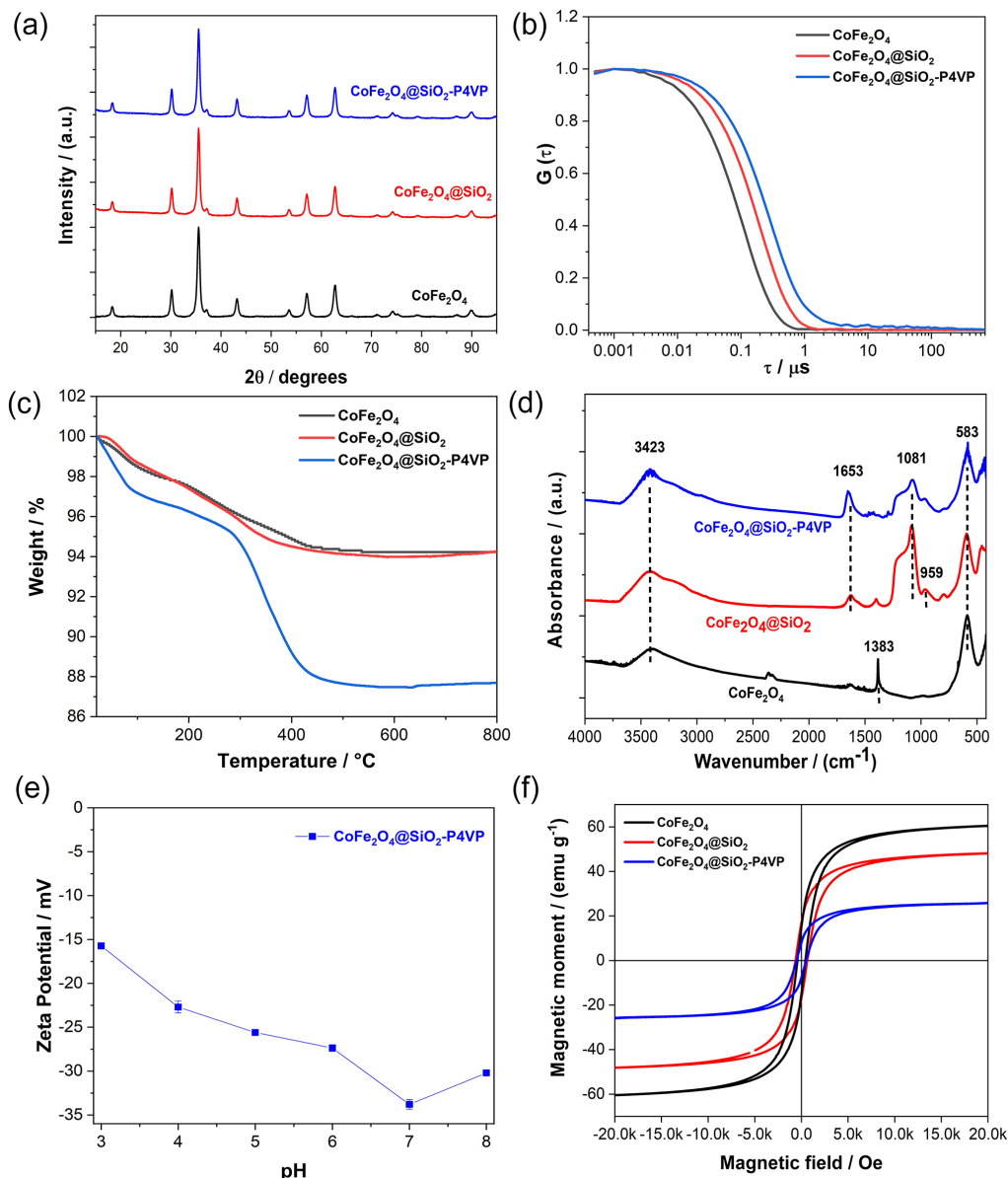
**Figure 2.** (a) XRD, (b) correlation function, (c) thermogravimetric curve, (d) IR (KBr) spectra, (e) zeta potential in pH function and (f) magnetization curve of $CoFe_2O_4$, $CoFe_2O_4@SiO_2$ and $CoFe_2O_4@SiO_2$-P4VP.

surface. The second loss (between 200 and 400 °C) refers to the loss of TEOS that may have remained on the silica surface due to incomplete hydrolysis, and also the residual –OH groups may be associated with the loss of ethanol from the TEOS that was not completely hydrolyzed.[50] P4VP was quantitatively evaluated on the $CoFe_2O_4@SiO_2$-P4VP material. The polymer degradation temperature was observed as a well-defined drop of 9.3% (by mass) at 380 °C (Table S2, SI section). Ko *et al.*[51] developed a silica particle followed by the polymerization of P4VP, using organic solvents and a reaction time of 24 h. The authors reported a mass percentage of 5%.[51] In the present study, the percentage of polymer mass inserted was 9.3% (Table S2).

Infrared spectra of the nanomaterials based on $CoFe_2O_4$ are presented in Figure 2d. For $CoFe_2O_4$, infrared bands near 400 and 600 cm⁻¹ indicate cation-anion interaction in octahedral and tetrahedral sites, respectively. These signals are characteristic of spinel structures, especially ferrites.[43] The signal near 1378 cm⁻¹ was attributed to an asymmetric axial deformation of –NO, indicating some residual nitrate from the passivation of the $CoFe_2O_4$ surface.[52] For the sample covered with a silica shell ($CoFe_2O_4@SiO_2$) and its analog containing the polymer ($CoFe_2O_4@SiO_2$-P4VP), the peak absorption near 1081 cm⁻¹ corresponds to the asymmetric deformation of Si–O–Si, the band near 960 cm⁻¹ is due to Si–O–H, and the SiO₂ ring vibration occurred at about 800 cm⁻¹.[53] At Figure 2d, the band referring to the $CoFe_2O_4@SiO_2$-P4VP spectrum at 1653 cm⁻¹ corresponds

to the elongation of the polymer's C–N. In addition, there is an increase in the intensity of the band by 3490 cm$^{-1}$ with a small displacement indicating hydrogen bonds. The main stretches of the materials are contained in Table S3 of the SI section. The presence of a shoulder around 1200-1000 cm$^{-1}$ can be related to the angular folding in the aromatic plane.

The ferrofluid suspensions present good physical stability, as the values of zeta potential (see $\zeta$ in Table 1) are higher than +30.0 mV. The positive zeta potential is due to the fact that the suspensions are prepared in strongly acidic media provided by nitric acid, where the surface sites are completely protonated.[54] After hydrolysis and condensation of TEOS at the surface of $CoFe_2O_4$@$SiO_2$, the amorphous silica shell provides deprotonated silanol groups that grant a negatively charged nanocomposite, which agrees with negative zeta potential values. The negative zeta potential of the polymer nanocomposites indicates that there is remaining deprotonated silanol on the surface. The curve of zeta potential in function of pH (Figure 2e) for $CoFe_2O_4$@$SiO_2$-P4VP indicated a negative surface of material in the solution.

All evaluated systems containing coating showed negative surface electrical density. The inversion of the charge polarity when compared to the pure nanoparticle is due to the presence of ionized silanol groups from silica, at the evaluated pH (pH 6.0). In the presence of P4VP, part of the charges are shielded due to the protonated nitrogen of the pyridine ring.[47]

## Magnetic properties

Figure 2f shows the magnetization curves *vs.* applied field that were recorded at 300 K for the bare and covered prepared nanomaterials. The VSM curve for bare $CoFe_2O_4$ nanoparticles shows a hysteresis loop with remanence of 14.9 emu g$^{-1}$ and coercivity of 426 Oe. These results indicate ferrimagnetic behavior, since at room temperature $CoFe_2O_4$ is blocked (constant magnetization). This behavior is in accordance with some studies already reported in the literature, where $CoFe_2O_4$ has high coercivity and is classified as a hard ferrite.[24,55,56] The reduction in the $M_S$ value, when compared to pure cobalt ferrite, can be attributed to the combination of surface effects. The non-magnetic material that has been deposited may have destabilized the collinear spin arrangement that produces several inclined and random spin structures on the surface.[24,56] DC magnetic susceptibility for the as-prepared nanoparticle sample was calculated considering the maximum point of the derivative $\chi = dM/dH$. For $CoFe_2O_4$, magnetic susceptibilities were $1.36 \times 10^{-2}$, $6.76 \times 10^{-2}$ emu g$^{-1}$ Oe$^{-1}$. The saturation magnetization is usually the parameter used to verify the ability to separate

the adsorbent nanoparticles from the solution, using a permanent magnet.[57-60]

A decrease in the $M_S$ value for $CoFe_2O_4$@$SiO_2$ and $CoFe_2O_4$@$SiO_2$-P4VP is observed when compared to the pure nanoparticle. The reduction in the $M_S$ value can be attributed to the surface effect that destabilizes the collinear spin array and produces several inclined and spin structures.[61] In addition, the incorporation of a non-magnetic material on the surface directly influences the magnetic content of the core-shell material. The nanomaterial $CoFe_2O_4$@$SiO_2$-P4VP prepared in the present study presented $M_S$ higher than 25.6 emu g$^{-1}$ at 300 K. For comparison, Yamini *et al.*[60] evaluated surface-modified magnetic silica to extract plasticizers from water samples, using $Fe_3O_4$ nanoparticles as core magnetic material.[60] The prepared nanomaterial presented $M_S$ of 21 emu g$^{-1}$, and the authors indicated that this value is favorable, and that the material could be dispersed in the water sample and conveniently isolated from it using an external magnet.[7,60]

## Application of nanomaterials in adsorption

### Evaluation of adsorption capacity

To verify the adsorption capacity of the prepared nanomaterials, the same adsorption conditions were applied to evaluate the amount of BPA removed from water at pH 6.0. The initial concentration of the analyte was 100.0 mg L$^{-1}$. Figure 3a indicates the adsorption capacity for each nanomaterial, namely $CoFe_2O_4$@$SiO_2$ and $CoFe_2O_4$@$SiO_2$-P4VP.

The nanomaterials functionalized with the P4VP group presented a higher performance when compared to the polymeric ones, with an adsorption capacity of 43 mg g$^{-1}$ of BPA from water. The materials with a silica shell did not present a significant adsorption capacity.[24] Due to the hydrophobic character of bisphenol A, there was little interaction with the adsorbent not modified with P4VP. This polar character of the silica surface promotes the stability of the nanoparticle in water and disfavors the adsorption of compounds of lipophilic character.[24,62] The results presented in the following items refer to the performance of the nanomaterial $CoFe_2O_4$@$SiO_2$-P4VP.

### Response surface

With the responses of adsorption capacity of BPA, an adjustment of the data to a quadratic model was performed, as described in Figure 3b. Table S4 (SI section) shows the analysis of variance (ANOVA) of each variable in the response. Figure 3b shows the observed response surface of the model. The analysis of variance presented in Table S4 and Figure 3c shows that the regression of the factors is

significant and that the lack of adjustment is not significant. Most of the model's residues are attributed to pure error (MQ$_{error}$ > MQ$_{lack\ of\ adjustment}$), which corroborates the good quality of the model. The statistical analysis of the data indicates that the quadratic model presented a percentage of explained correlation R = 0.88187.[22,35] Thus, 88.19% of the variations in responses can be explained by factors, that is, they can be explained by the model's indicated function with significant terms for equation 12.

$$Q_e = -77.5 + 25.7(pH) + 34.5([NaCl])  \qquad (12)$$

The significant factors for BPA adsorption, at a confidence level of 95%, can be seen in *p* > 0.05 in Figure 3c. Figure 3d shows the values predicted by the model and the experimental values. As indicated in Table S4, the lack of model fit was not significant. Both factors are linearly significant with a positive effect. Through the analysis of the contour surface, it is possible to observe that the greatest response, that is, greater adsorption of the 46.6 mg g$^{-1}$ capacity, occurs at pH 7.15 and ionic strength 1.71 mol L$^{-1}$. These results are in agreement with univariate experiments.[63,64]
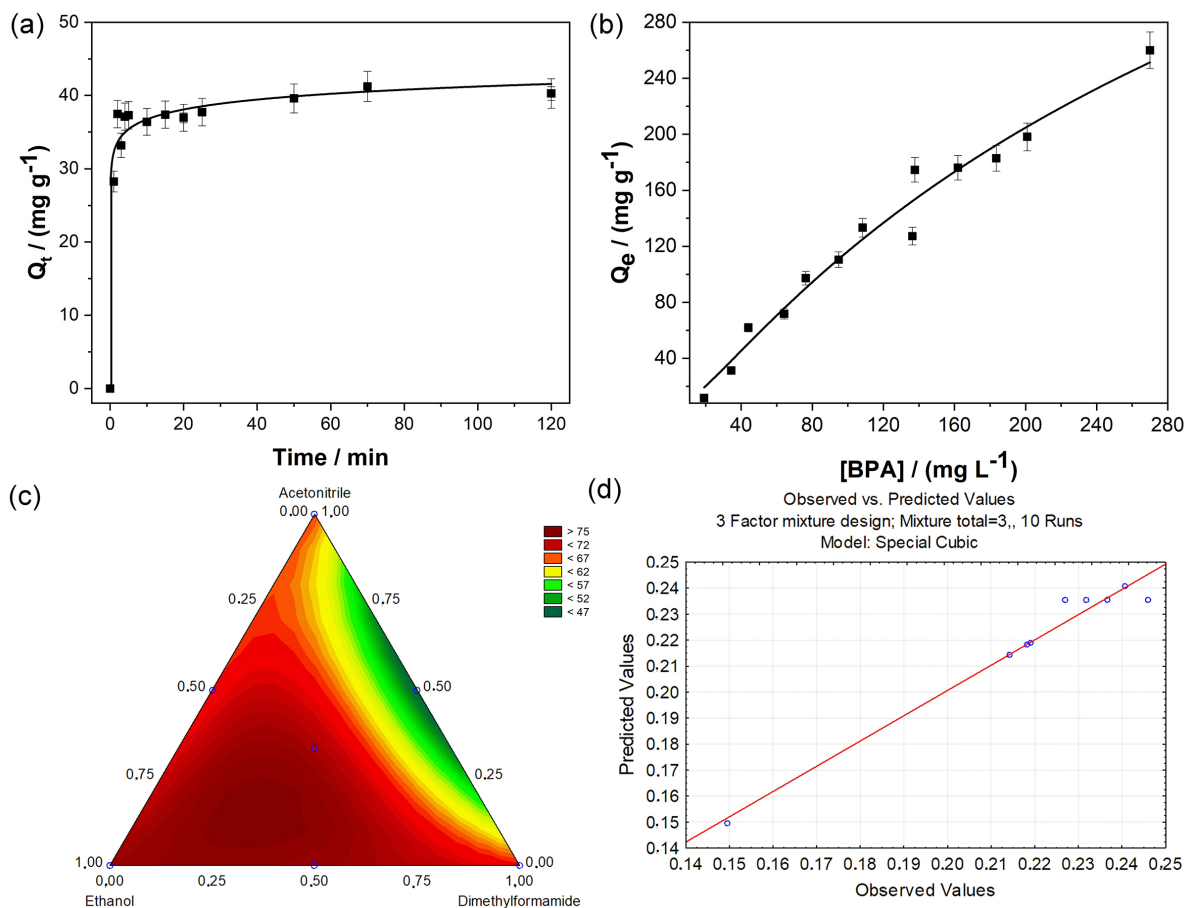
## Adsorption kinetics

To check the shortest shaking time needed, a kinetics experiment was carried out after the solution with the analyte had been previously kept in contact with the magnetic extractor for 10 min under sonication, for better dispersion of CoFe$_2$O$_4$@SiO$_2$-P4VP in the solution. After that period, the samples were agitated for various periods and aliquots were collected and analyzed. An exponential growth adjusted the kinetics data, presented in Figure 4a.

In the present study, no activation step was employed. The initial concentration of the analyte was 100.0 mg L$^{-1}$ and 5 mg of adsorbent was used. To elucidate the mechanisms of the adsorption process, non-linear models of pseudo-first and pseudo-second order and linear models of Elovich and intraparticle diffusion were applied to experimental data, and their respective parameters are presented in Table 2.

For nanocomposite CoFe$_2$O$_4$@SiO$_2$-P4VP, the pseudo-second order model was well adjusted to the experimental data, considering the high values of regression coefficients (R$^2$), and the similarity of experimental adsorption (Q$_e$) was well adjusted to the response surface model. The pseudo-
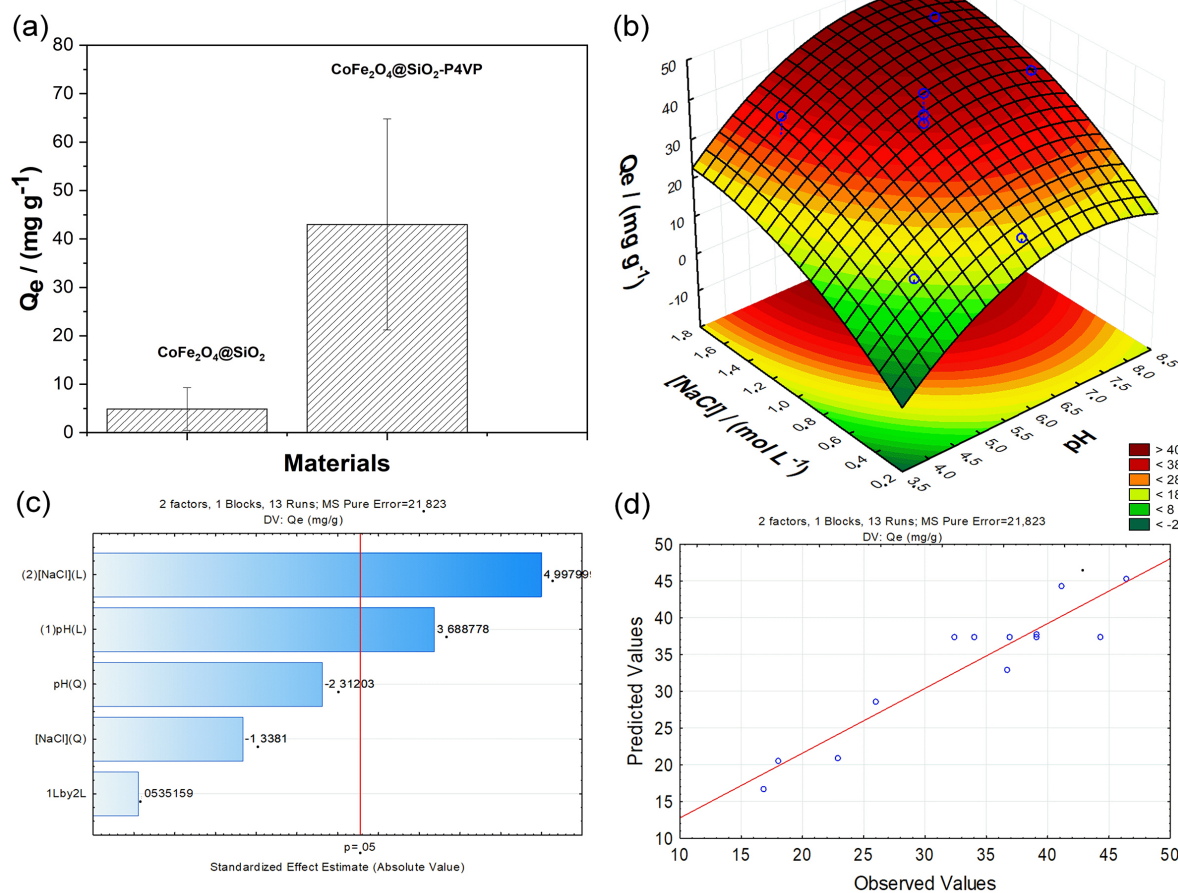


**Figure 3.** (a) Adsorption capacity comparison. (b) Surface response of adsorption capacity of bisphenol A in function of pH and ionic force. (c) Effect estimate for adsorption capacity for BPA in function pH and [NaCl]; (d) observed *vs.* predicted values of surface response.

**Figure 4.** (a) Kinetic and (b) isotherm adsorption of BPA in CoFe$_2$O$_4$@SiO$_2$-P4VP at 25 °C. (c) Diagram ternary of desorption. (d) Observed *vs.* predicted values of ternary diagram of desorption.

**Table 2.** Kinetic parameters for BPA adsorption in CoFe$_2$O$_4$@SiO$_2$-P4VP

| Pseudo-first order | | | Pseudo-second order | | | Elovich | | | Intraparticle | | |
|---|---|---|---|---|---|---|---|---|---|---|---|
| $k_1$ / min$^{-1}$ | $Q_{ad}$ / (mg g$^{-1}$) | $R^2$ | $k_2$ / (g mg$^{-1}$ min$^{-1}$) | $Q_{ad}$ / (mg g$^{-1}$) | $R^2$ | $\alpha$ / (min$^{-1}$ mg g$^{-1}$) | $\beta$ / (g mg$^{-1}$) | $R^2$ | $k_{id}$ / (mg g$^{-1}$ min$^{-1/2}$) | CL / (mg g$^{-1}$) | $R^2$ |
| 8.9E-2 | 67.1 | 0.755 | 59.9 | 40.6 | 0.999 | 2.3E7 | 0.5 | 0.623 | 1.94 | 26.9 | 0.321 |

$k_1$: adsorption rate constant for pseudo-first order; $Q_{ad}$: amount adsorbed; $R^2$: coefficient of determination; $k_2$: adsorption rate constant for pseudo-second order; $\alpha$: initial rate of adsorption; $\beta$: desorption constant; $k_{id}$: intraparticle diffusion constant; CL: boundary layer effect thickness.

second order model predicts the presence of adsorption sites with different energies. These systems are characteristics with heterogeneous surface.[65,66] Before equilibrium, the adsorption process occurs in more available sites, according to the model. Adsorption coating P4VP adsorbent generally kinetic of pseudo-second order model presented good correlation.[30,67]

Adsorption isotherm

Adsorption isotherm models are usually used to indicate the equilibrium of the interaction and adsorption process. The adsorption isotherms were obtained at 298 K. Figure 4b shows the adsorption isotherm of BPA on as-prepared CoFe$_2$O$_4$@SiO$_2$-P4VP. In this study, the Langmuir, Freundlich and Temkin models were used to fit the adsorption isotherms for the adsorbate. The Langmuir and Freundlich isotherm models are often used to explain isotherms. While the Langmuir model assumes the adsorption of a monolayer without interaction between the adsorption sites, the Freundlich model is an empirical model that describes a multilayer adsorption process. The Temkin isotherm considers systems where there are significant interaction effects between the adsorbent and the adsorbate in the adsorption process.[65]

The adsorption isotherms of BPA with CoFe$_2$O$_4$@SiO$_2$-P4VP at temperatures ranging from 25 °C are shown in Figure 4b. The initial concentrations of BPA start at 100 mg L$^{-1}$.

**Table 3.** The results for different model isotherms at 298 K

| Model | Langmuir | | | Temkin | | | Freundlich | | |
|---|---|---|---|---|---|---|---|---|---|
| Isotherm results | $K_L$ | $Q_{max}$ / (mg g$^{-1}$) | R | $K_T$ | $b_T$ / (mg g$^{-1}$) | R | $K_F$ / [(mg g$^{-1}$) (L mg$^{-1}$)$^{1/n}$] | n | R |
| | 2500 | $3.92 \times 10^{-4}$ | 0.14 | 0.043 | 89.9 | 0.96 | 0.86 | 0.92 | 0.97 |

$K_L$: affinity constant for Langmuir isothermal model; $Q_{max}$: maximum amount adsorbed; R: coefficient of correlation; $K_T$: equilibrium bond constant for Temkin model; $b_T$: Temkin constant; $K_F$: Freundlich constant; n: adsorption intensity.

In Table 3, the correlation coefficient (R) value indicated a better fit using the Freundlich model. $K_F$ is the adsorption constant of the Freundlich model associated with the adsorption capacity of BPA by the nanocomposite. CoFe$_2$O$_4$@SiO$_2$-P4VP at equilibrium. The n value represents the heterogeneity surface.[66]

The combined results indicated the adsorption capacity of the heterogeneous surface.[64] Analysis showed that interactions between the π-π conjugate system and the amino group of CoFe$_2$O$_4$@SiO$_2$-P4VP were conducive to the adsorption of BPA, which was mainly caused by van der Waals forces and the π-π interactions of the BPA aromatic ring. The hydrogen bonding interaction and hydrophobic effect contributed to surface adsorption.[4,21,33] Similar values of $K_F$ and n were found at a temperature of 25 °C by Ou *et al.*[68] In Table 4, the BPA adsorption capacity values in different materials are shown.

**Table 4.** The comparison for adsorption capacity for BPA in different materials

| Material | $Q_e^c$ / (mg g$^{-1}$) | Reference |
|---|---|---|
| CoFe$_2$O$_4$@SiO$_2$-P4VP | 46.6 | this study |
| Copolymer[a] | 50.4 | Lv *et al.*[2] |
| Fe$_3$O$_4$@COF[b] | 38.9 | Chen *et al.*[4] |
| Graphene oxide | 41.3 | Bai *et al.*[5] |
| Activated carbon | 210 | Hernández-Abreu *et al.*[63] |

[a]Hydroxypropyl-β-cyclodextrin copolymer; [b]covalent organic framework (COF)-1,3,5-tris(4-aminophenyl)benzene and terephthaldicarboxaldehyde copolymer; [c]adsorption capacity values in different materials.

### Desorption

The desorption study of the BPA from the adsorbent was carried out using mixtures of solvents, arranged in a ternary diagram. The solvents were chosen according to the study developed by Sun *et al.*[69] The percentage of desorption found for the different proportions of EtOH, ACN and DMF are presented in Figure 4c. The special cubic model of triangular surface indicated the function with significant terms in equation 13.

Percentage of desorption = 75.4(EtOH) +
68.6(DMF) + 67.1(ACN) − 84.2(DMF)(ACN) +
337.5(EtOH)(DMF)(ACN)      (13)

The analysis of variance (ANOVA) presented in Table S5 (SI section) shows that the regression of the factors is significant and that the lack of fit is not significant. Most of the model's residues are attributed to pure error ($MS_{error} > MS_{lack\ of\ fit}$), which corroborates the good quality of the model.[24,35] The statistical analysis of the data indicates that the quadratic model presented a percentage of explained correlation with R = 0.97165. Thus, 97.16% of the variations in responses can be explained by specific factors indicated in equation 13. In Figure S1 (SI section), the Pareto chart indicates the effect of each variable and the combination of them in the percentage desorption response. It is observed that all the pure solvents used had significant and positive effects, that is, they contributed to increasing the desorption percentage of BPA. A negative contribution when DMF:ACN are used indicating that they contribute in a way to decrease the percentage desorption.[24] The ternary mixture between EtOH:DMF:ACN has a significant and positive contribution to the desorption of BPA. Figure 4d shows the observed values *versus* the values predicted by the model.

The maximum desorption of BPA in the mixture was found in the proportion 1:2:5 for ACN:DMF:EtOH. These results indicate the influence of the condition of a good solvent for the adsorbate, such as DMF, for BPA and the presence of ethanol as a solvent for both BPA and for the adsorbent, since EtOH promotes the opening of the polymeric structure of P4VP.[42,70]

### Cycles of nanomaterial reuse

Reusability is an important factor for the utility of adsorption materials (see Figure S2b, SI section). The adsorption-desorption cycle was repeated 8 times using the CoFe$_2$O$_4$@SiO$_2$-P4VP nanocomposites. As shown in Figure S2, CoFe$_2$O$_4$@SiO$_2$-P4VP remained stable for up to 8 adsorption cycles, with only a slight decrease in adsorption capacities.[1,21,33] The results indicated that the CoFe$_2$O$_4$@SiO$_2$-P4VP nanocomposites had reusability and chemical stability. Thus, the nanocomposite of CoFe$_2$O$_4$@SiO$_2$-P4VP has strong potential to be used as a magnetic adsorbent of BPA from aqueous environmental samples.

## Conclusions

This study described the preparation and application of core-shell $CoFe_2O_4$-based magnetic nanoparticles coated with a surface-modified silica shell as a magnetic adsorbent of bisphenol A in water. The preparation of the nanomaterials involved the synthesis of $CoFe_2O_4$ by co-precipitation, followed by the preparation of the core-shell nanoparticle. The silica layer was deposited on the surface using a sol-gel process. The polymeric shell of P4VP was synthesized via miniemulsion radical polymerization. The characterizations confirm that the nanostructured materials present magnetization and decoration, which makes them suitable for the planned application. The decoration with the polymer on the silica was essential to adsorb the bisphenol A from the aqueous solution. The BPA adsorption capacity by the $CoFe_2O_4@SiO_2$-P4VP material was optimized with respect to pH and ionic strength through a feedback surface. BPA adsorption was optimized by the response surface method with good correlation (R > 0.88). Under the conditions of pH 7.15 and ionic strength of 1.71 mol L$^{-1}$, an adsorption capacity of 46.6 mg g$^{-1}$ was obtained. Under the optimized conditions, the adsorption kinetics of BPA indicated a pseudo-second order process. The Freundlich isotherm was the most adequate to fit the data, indicating a multilayer adsorption process. The desorption optimization through a ternary mixture diagram between the solvents DMF, EtOH and ACN showed a very strong correlation (R > 0.97) and maximum desorption in the proportions 1:2:5 of ACN:DMF:EtOH. The adsorbent efficiency showed up to eight reuse cycles. These characteristics, associated with the characteristics of nanocomposites in terms of size, magnetic properties and adsorption capacity, allow a potential application of this system in the removal of BPA from the aqueous medium.

## Supplementary Information

Supplementary data (levels of variation, stages of thermal degradation, stretch FTIR, adsorption capacity comparison, ANOVA for response surface adsorption and desorption, effect estimate, calibration curve and parameters of curve) are available free of charge at http://jbcs.sbq.org.br as a PDF file.

## Acknowledgments

## Author Contributions

The manuscript was written using contributions from all the authors. All the authors have given approval to the final version of the manuscript.

## References

1. Zhou, Q.; Lei, M.; Wu, Y.; Zhou, X.; Wang, H.; Sun, Y.; Sheng, X.; Tong, Y.; *Chemosphere* **2020**, *238*, 124621. [Crossref]

2. Lv, Y.; Ma, J.; Liu, K.; Jiang, Y.; Yang, G.; Liu, Y.; Lin, C.; Ye, X.; Shi, Y.; Liu, M.; Chen, L.; *J. Hazard. Mater.* **2021**, *403*, 123666. [Crossref]

3. Prete, M. C.; Tarley, C. R. T.; *Chem. Eng. J.* **2019**, *367*, 102. [Crossref]

4. Chen, L.; He, Y.; Lei, Z.; Gao, C.; Xie, Q.; Tong, P.; Lin, Z.; *Talanta* **2018**, *181*, 296. [Crossref]

5. Bai, X.; Qin, C.; Feng, R.; Ye, Z.; *Mater. Chem. Phys.* **2017**, *189*, 96. [Crossref]

6. Ahsan, M. A.; Jabbari, V.; Islam, M. T.; Turley, R. S.; Dominguez, N.; Kim, H.; Castro, E.; Hernandez-Viezcas, J. A.; Curry, M. L.; Lopez, J.; Gardea-Torresdey, J. L.; Noveron, J. C.; *Sci. Total Environ.* **2019**, *673*, 306. [Crossref]

7. Santhosh, C.; Daneshvar, E.; Kollu, P.; Peräniemi, S.; Grace, A. N.; Bhatnagar, A.; *Chem. Eng. J.* **2017**, *322*, 472. [Crossref]

8. Ali, N.; Hassan Riead, M. M.; Bilal, M.; Yang, Y.; Khan, A.; Ali, F.; Karim, S.; Zhou, C.; Wenjie, Y.; Sher, F.; Iqbal, H. M. N.; *Chemosphere* **2021**, *284*, 131279. [Crossref]

9. Wang, X.; Ou, H.; Huang, J.; *J. Colloid Interface Sci.* **2019**, *538*, 499. [Crossref]

10. Keçili, R.; Ghorbani-Bidkorbeh, F.; Dolak, İ.; Canpolat, G.; Karabörk, M.; Hussain, C. M.; *TrAC, Trends Anal. Chem.* **2021**, *143*, 116380. [Crossref]

11. Wang, Y.; Gao, Z.; Shang, Y.; Qi, Z.; Zhao, W.; Peng, Y.; *Chem. Eng. J.* **2020**, *417*, 128063. [Crossref]

12. Behrens, S.; Appel, I.; *Curr. Opin. Biotechnol.* **2016**, *39*, 89. [Crossref]

13. Ghosh Chaudhuri, R.; Paria, S.; *Chem. Rev.* **2012**, *112*, 2373. [Crossref]

14. Sodipo, B. K.; Aziz, A. A.; *J. Magn. Magn. Mater.* **2016**, *416*, 275. [Crossref]

15. Liberman, A.; Mendez, N.; Trogler, W. C.; Kummel, A. C.; *Surf. Sci. Rep.* **2014**, *69*, 132. [Crossref]

16. Vasconcelos, I.; Fernandes, C.; *TrAC, Trends Anal. Chem.* **2017**, *89*, 41. [Crossref]

17. Fan, Y.-H.; Zhang, S.-W.; Qin, S.-B.; Li, X.-S.; Zhang, Y.; Qi, S.-H.; *Anal. Bioanal. Chem.* **2017**, *409*, 3337. [Crossref]

18. Li, Y.; Wang, Y.; Lu, H.; Li, X.; *Int. J. Hydrogen Energy* **2020**, *45*, 16080. [Crossref]

19. Guo, W.; Wang, G.; Wang, Q.; Dong, W.; Yang, M.; Huang, X.; Yu, J.; Shi, Z.; *J. Mol. Catal. A: Chem.* **2013**, *378*, 344. [Crossref]

20. Miao, Z.; Shu, X.; Ramella, D.; *RSC Adv.* **2017**, *7*, 2773. [Crossref]

21. Li, Q.; Pan, F.; Li, W.; Li, D.; Xu, H.; Xia, D.; Li, A.; *Polymers (Basel)* **2018**, *10*, 1136. [Crossref]

22. Bezerra, M. A.; Santelli, R. E.; Oliveira, E. P.; Villar, L. S.; Escaleira, L. A.; *Talanta* **2008**, *76*, 965. [Crossref]

23. Nissy, S. M.; Surendra, B.; Raju, K. D.; Vangalapati, M.; *Mater. Today: Proc.* **2018**, *5*, 17914. [Crossref]

24. Caon, N. B.; Cardoso, C. D. S.; Faita, F. L.; Vitali, L.; Parize, A. L.; *J. Environ. Chem. Eng.* **2020**, *8*, 104003. [Crossref]

25. Pinho, S. L. C.; Pereira, G. A.; Voisin, P.; Kassem, J.; Bouchaud, V.; Etienne, L.; Peters, J. A.; Carlos, L.; Mornet, S.; Geraldes, C. F. G. C.; Rocha, J.; Delville, M.-H.; *ACS Nano* **2010**, *4*, 5339. [Crossref]

26. Medeiros, A. M. M. S.; Parize, A. L.; Oliveira, V. M.; Neto, B. A. D.; Bakuzis, A. F.; Sousa, M. H.; Rossi, L. M.; Rubim, J. C.; *ACS Appl. Mater. Interfaces* **2012**, *4*, 5458. [Crossref]

27. Qiao, Z.; Perestrelo, R.; Reyes-Gallardo, E. M.; Lucena, R.; Cárdenas, S.; Rodrigues, J.; Câmara, J. S.; *J. Chromatogr. A* **2015**, *1393*, 18. [Crossref]

28. Rasband, W. S.; *ImageJ*; U. S. National Institutes of Health, Bethesda, Maryland, USA, 2014.

29. TIBCO Software; *Statistica*, version 13.5.0.17; TIBCO Software Inc., Palo Alto, CA, USA, 2018.

30. Ngoc, P. K.; Mac, T. K.; Nguyen, H. T.; Viet, D. T.; Thanh, T. D.; Van Vinh, P.; Phan, B. T.; Duong, A. T.; Das, R.; *J. Sci.: Adv. Mater. Devices* **2022**, *7*, 100438. [Crossref]

31. Duarte Neto, J. F.; Pereira, I. D. S.; da Silva, V. C.; Ferreira, H. C.; Neves, D. G. A.; Menezes, R. R.; *Ceramica* **2018**, *64*, 598. [Crossref]

32. Özcan, A. S.; Özcan, A.; *J. Colloid Interface Sci.* **2004**, *276*, 39. [Crossref]

33. You, L.; Xu, K.; Ding, G.; Shi, X.; Li, J.; Wang, S.; Wang, J.; *J. Mol. Liq.* **2020**, *320*, 114456. [Crossref]

34. Borhan, A.; Yusup, S.; Lim, J. W.; Show, P. L.; *Processes* **2019**, *7*, 855. [Crossref]

35. Wang, X.; Chen, A.; Chen, B.; Wang, L.; *Ecotoxicol. Environ. Saf.* **2020**, *204*, 111093. [Crossref]

36. Quan, L. D.; Dang, N. H.; Tu, T. H.; Phuong Linh, V. N.; Mong Thy, L. T.; Nam, H. M.; Phong, M. T.; Hieu, N. H.; *Synth. Met.* **2019**, *255*, 116106. [Crossref]

37. Dada, A. O.; Olaken, A. P.; Olatunya, A. M.; Dada, O.; *IOSR J. Appl. Chem.* **2012**, *3*, 38. [Crossref]

38. Ragavan, K. V.; Rastogi, N. K.; *Carbohydr. Polym.* **2017**, *168*, 129. [Crossref]

39. Badley, R. D.; Ford, W. T.; McEnroe, F. J.; Assink, R. A.; *Langmuir* **1990**, *6*, 792. [Crossref]

40. Zhou, L.; Li, N.; Owens, G.; Chen, Z.; *Chem. Eng. J.* **2019**, *362*, 628. [Crossref]

41. Rodovalho, F. L.; Capistrano, G.; Gomes, J. A.; Sodré, F. F.; Chaker, J. A.; Campos, A. F. C.; Bakuzis, A. F.; Sousa, M. H.; *Chem. Eng. J.* **2016**, *302*, 725. [Crossref]

42. Kevadiya, B. D.; Bade, A. N.; Woldstad, C.; Edagwa, B. J.; McMillan, J. E. M.; Sajja, B. R.; Boska, M. D.; Gendelman, H. E.; *Acta Biomater.* **2017**, *49*, 507. [Crossref]

43. Safi, R.; Ghasemi, A.; Shoja-Razavi, R.; Ghasemi, E.; Sodaee, T.; *Ceram. Int.* **2016**, *42*, 6375. [Crossref]

44. Ferreira, T. A. S.; Waerenborgh, J. C.; Mendonça, M. H. R. M.; Nunes, M. R.; Costa, F. M.; *Solid State Sci.* **2003**, *5*, 383. [Crossref]

45. Uvarov, V.; Popov, I.; *Mater. Charact.* **2007**, *58*, 883. [Crossref]

46. Lim, J.; Yeap, S. P.; Che, H. X.; Low, S. C.; *Nanoscale Res. Lett.* **2013**, *8*, 381. [Crossref]

47. Clara-Rahola, J.; Moscoso, A.; Belén Ruiz-Muelle, A.; Laurenti, M.; Formanek, P.; Lopez-Romero, J. M.; Fernández, I.; Diaz, J. F.; Rubio-Retama, J.; Fery, A.; Contreras-Cáceres, R.; *J. Colloid Interface Sci.* **2018**, *514*, 704. [Crossref]

48. Tourinho, F.; Franck, R.; Massart, R.; Perzynski, R. In *Trends in Colloid and Interface Science III*, vol. 134; Bothorel, P.; Dufourc, E. J., eds.; Steinkopff: Darmstadt, 2007, p. 128-134. [Crossref]

49. Bunaciu, A. A.; Udriştioiu, E. G.; Aboul-Enein, H. Y.; *Crit. Rev. Anal. Chem.* **2015**, *45*, 289. [Crossref]

50. Nassor, E. C. O.; Ávila, L. R.; Pereira, P. F. S.; Ciuffi, K. J.; Calefi, P. S.; Nassar, E. J.; *Mater. Res.* **2011**, *14*, 1. [Crossref]

51. Ko, T.; Kim, K.; Kim, S. K.; Lee, J. C.; *Polymer (Guildf)* **2015**, *71*, 70. [Crossref]

52. Jacob, B. P.; Kumar, A.; Pant, R. P.; Singh, S.; Mohammed, E. M.; *Bull. Mater. Sci.* **2011**, *34*, 1345. [Crossref]

53. Iqbal, Y.; Bae, H.; Rhee, I.; Hong, S.; *J. Magn. Magn. Mater.* **2016**, *409*, 80. [Crossref]

54. Tourinho, F. A.; Campos, A. F. C.; Aquino, R.; Lara, M. C. F. L.; da Silva, G. J.; Depeyrot, J.; *Braz. J. Phys.* **2002**, *32*, 501. [Crossref]

55. Rao, K. S.; Choudary, G. S. V. R. K.; Rao, K. H.; Sujatha, C.; *Procedia Mater. Sci.* **2015**, *10*, 19. [Crossref]

56. Stein, C. R.; Bezerra, M. T. S.; Holanda, G. H. A.; André-Filho, J.; Morais, P. C.; *AIP Adv.* **2018**, *8*, 056303. [Crossref]

57. Mohammadi, A.; Daemi, H.; Barikani, M.; *Int. J. Biol. Macromol.* **2014**, *69*, 447. [Crossref]

58. Huang, C.; Wang, Y.; Huang, Q.; He, Y.; Zhang, L.; *Anal. Chim. Acta* **2019**, *1054*, 38. [Crossref]

59. Boon, Y. H.; Mohamad Zain, N. N.; Mohamad, S.; Osman, H.; Raoov, M.; *Food Chem.* **2019**, *278*, 322. [Crossref]

60. Yamini, Y.; Faraji, M.; Adeli, M.; *Microchim. Acta* **2015**, *182*, 1491. [Crossref]

61. Tenório-Neto, E. T.; Jamshaid, T.; Eissa, M.; Kunita, M. H.; Zine, N.; Agusti, G.; Fessi, H.; El-Salhi, A. E.; Elaissari, A.; *Polym. Adv. Technol.* **2015**, *26*, 1199. [Crossref]

62. Godiya, C. B.; Park, B. J.; *Environ. Chem. Lett.* **2022**, *20*, 1801. [Crossref]

63. Hernández-Abreu, A. B.; Álvarez-Torrellas, S.; Rocha, R. P.; Pereira, M. F. R.; Águeda, V. I.; Delgado, J. A.; Larriba, M.; García, J.; Figueiredo, J. L.; *Appl. Surf. Sci.* **2021**, *552*, 149513. [Crossref]

64. Jin, Q.; Zhang, S.; Wen, T.; Wang, J.; Gu, P.; Zhao, G.; Wang, X.; Chen, Z.; Hayat, T.; Wang, X.; *Environ. Pollut.* **2018**, *243*, 218. [Crossref]

65. Zhou, Q.; Wang, Y.; Xiao, J.; Fan, H.; *Synth. Met.* **2016**, *212*, 113. [Crossref]

66. Raza, S.; Wen, H.; Peng, Y.; Zhang, J.; Li, X.; Liu, C.; *Eur. Polym. J.* **2021**, *144*, 110199. [Crossref]

67. Tian, T.; Liu, M.; Li, Y.; Han, J.; Ren, L.; Lorenz, H.; Wu, Q.; Chen, J.; *Particuology* **2021**, 124562. [Crossref]

68. Ou, Y.-H.; Chang, Y.-J.; Lin, F.-y.; Chang, M.-l.; Yang, C.-Y.; Shih, Y.-h.; *Ecol. Eng.* **2016**, *92*, 270. [Crossref]

69. Sun, J.; Wang, L.; Ding, S.; Sun, X.; Xu, L.; *J. Chem. Eng. Data* **2020**, *65*, 2846. [Crossref]

70. Kumar, L.; Horechyy, A.; Bittrich, E.; Nandan, B.; Uhlmann, P.; Fery, A.; *Polymers (Basel)* **2019**, *11*, 1882. [Crossref]